A Model of RF Heating around DBS leads

Predicting MRI RF heating in DBS patients for image optimization using 3D Gradient echo scans and an anthropomorphic phantom

University of Twente
Magnetic Detection & Imaging

Erik Arts
Bachelor Thesis BMT
June 28, 2024

Prof. dr ir. B. ten Haken	Dr. ir. W. M. Brink	Dr. M. C. Piastra
Head of committee	Mentor	External Member

UNIVERSITEIT TWENTE.
Opleiding BSc Biomedische Technologie

Acknowledgement

This paper would not have been possible if not for the help of some great people. First, I would like to express my gratitude to Wyger Brink, my mentor for my Bachelor Thesis. Weekly meetings and discussions with him have greatly enhanced my learning and were crucial to the successful completion of this project. His guidance and extensive knowledge on the topic proved invaluable. But not only was he my mentor, he also sprouted my enthusiasm for Magnetic Resonance Imaging during his lectures on the subject.

Furthermore, I am thankful to Maria Carla Piastra for the feedback she provided. Her perspectives allowed me to clarify and restructure various sections of my report. Additional feedback was provided by my father, Technical Medicine student Daphne van Veenendaal and Embedded Systems student Willem van Dijk, for which my thanks.

Moreover, I wish to thank Bennie ten Haken, the chair of my committee, for accepting my thesis and providing feedback. I am also grateful to Jauke Reinders, a master student working on a closely related topic. I am excited to see where his work with the phantom leads, and I wish him the best of luck. Finally, I would like to acknowledge the support provided by my family and friends throughout this project. I am deeply grateful to you all.

Summary

This study aims to give insight into a method to create patient specific scanning protocols to improve possibilities for clinical magnetic resonance imaging (MRI) scans in deep brain stimulation (DBS) patients. In these patients, radio frequency heating around electrodes poses mayor safety concerns [1]. To evaluate safe scanning parameters, a modelling strategy is applied and validated in a phantom.

The key scanning parameter evaluated in this paper is the repetition time (TR): the interval between two consecutive excitation pulses. Increasing TR allows more heat dissipation, resulting in a lower end temperature. However, increasing TR also increases overall scan time. To remain clinically viable, the scan time cannot be extended indefinitely. A predictive model allows for the selection of an optimal TR that ensures scan safety while not unnecessarily prolonging the scan time.

The model comprises two main components: calibration data and a scaling parameter. The calibration data provides the general shape of the heating curve. To obtain this, an agar phantom is scanned. The obtained curve features the temperature over time for a given sequence and configuration, which can be scaled to conform other sequences and configurations. To accurately scale the calibration curve, the orientation-specific heating is quantified using a 3D Gradient Echo scan. By analysing the location of the transmission magnetic field null artifact relative to the electrodes, the induced current is determined [2]. The power deposition of this current causes the RF heating, commonly represented using the Specific Absorption Rate (SAR). Knowledge on the magnitude of the induction current provides the necessary scaling factor.

Scaling the curve provides rapid and accurate data relating repetition time to tissue heating. By abstaining from computationally heavy simulations, the model can give quick feedback to ensure smooth MRI operation. To maintain accuracy, calibration data is to be obtained from high resemblance anthropomorphic phantoms or cadavers using clinically representative sequences, such as low-SAR (Siemens). Combined with RF heating mitigation strategies, this model could prove vital for improving clinical MRI scan accessibility for DBS patients.

Samenvatting

Deze studie tracht inzicht te geven in een methode om patiëntspecifieke scanprotocollen te creëren om klinische toepasbaarheid van MRI-scans in diepe hersenstimulatie (DBS) patiënten te verbeteren. Bij deze patiënten vormt radiofrequente opwarming een veiligheidsrisico [1]. Om veilige scanparameters te vinden, wordt een model toegepast en gevalideerd in een fantoom.

De belangrijkste scanparameter die in dit artikel wordt geëvalueerd, is de repetitietijd (TR): het interval tussen twee opeenvolgende excitatiepulsen. Het verhogen van de TR laat meer warmteafvoer toe, wat resulteert in een lagere eindtemperatuur. Het verhogen van de TR verlengd echter ook de totale scantijd. Om klinisch relevant te blijven, kan de scantijd niet oneindig verlegt worden. Een voorspellend model geeft de mogelijkheid om een optimale TR te kiezen die veiligheid biedt en de scantijd niet onnodig laat oplopen.

Het model bestaat uit twee hoofdcomponenten: een kalibratiecurve en een schaalparameter. De kalibratiedata geeft de algemene vorm van de te voorspellen verwarmingscurve. Om deze te verkrijgen, wordt een agar-fantoom gescand. De verkregen curve geeft temperatuur over tijd weer voor een gegeven sequentie en configuratie, deze kan worden geschaald naar andere sequenties en configuraties. Om de kalibratiecurve accuraat te schalen, wordt de oriëntatiespecifieke verwarming gekwantificeerd met behulp van een 3D Gradient Echo-scan. Door de locatie van het zend magnetisch veld nul-artefact ten opzichte van de elektroden te analyseren, wordt de geïnduceerde stroom bepaald [2]. Het vermogen van deze stroom die als hitte het weefsel inkomt, veroorzaakt de RF-verwarming. Deze opwarming wordt vaak aangeduid met de Specific Absorbtion Rate (SAR). Kennis van de magnitude van de inductiestroom levert de benodigde schaalfactor op.

Het schalen van de curve biedt snel en nauwkeurig inzicht met betrekking tot repetitietijd en weefselverwarming. Door computationeel zware simulaties te vermijden, kan het model snelle feedback geven om soepel MRI gebruik te bevorderen. Om de nauwkeurigheid te behouden, moeten kalibratiegegevens worden verkregen van gedetaillieerde antropomorfe fantomen of kadavers met behulp van klinisch representatieve sequenties, zoals low-SAR (Siemens). Gecombineerd met strategieën voor het beperken van RF-verwarming, kan dit model een cruciale rol spelen in het verbeteren van klinische MRI-scan toegankelijkheid voor DBS-patiënten.

Contents

Chapter 1

Introduction

Deep Brain Stimulation (DBS) is an invasive neurosurgical intervention for severe psychiatric and movement disorders such as Parkinson's disease, dystonia, treatment-refractory obsessive-compulsive disorder and more [3, 4]. First approved in 1990, the DBS apparatus consists of implanted electrodes that are connected to an implantable pulse generator via subcutaneous leads. The pulse generator sends electric pulses to specific deep brain nuclei. Hitting the exact stimulation location is crucial, missing by a millimetre can result in poor clinical outcomes [5]. DBS patients can significantly benefit from Magnetic Resonance Imaging (MRI), not only for electrode localization, but also for postoperative treatment monitoring [6, 7]. However, MRI scanning can pose a risk of permanent tissue damage in subjects with a DBS systems [1, 8]. MRI relies on the use of high energy radio frequency (RF) pulses to excite spins of hydrogen atoms. These RF magnetic fields can induce a current in conductive structures, such as DBS leads, leading to tissue heating. While energy deposition of these pulses occurs during normal scans, the DBS electrode greatly enhances the process. This is known as the 'antenna resonance effect' and is heavily influenced by the orientation of the electrode within the magnetic field [9]. This inherently presents us with a problem. How does one make a high resolution MRI scan while mitigating heating of the tissue caused by the electrodes?

Various solutions have been proposed, ranging from redesigning or altering the materials of the DBS system [10, 11], electric field tailoring [12, 13] to lowering the specific absorption rate (SAR) through RF shimming [14]. Regardless of all effort, no universal method has been established [15]. As orientation of the DBS electrodes varies largely between patients, a 'one-size-fits-all' solution is not easily found. It is therefore beneficial to aim for a patient specific solution. In order to accomplish this, models are needed to predict the RF heating in individual patients. A possible strategy could be by characterising the induction current that inherently causes the RF heating. This can be accomplished using a low SAR gradient echo (GRE) [2, 15]. Information on the induction current can be used to simulate the heating around the electrodes and even mitigate it. Current models allow accurate temperature prediction [16], but do not integrate it to find personalized excitation settings for safe clinical scanning.

In this paper, a model will be constructed to relate the induced current to RF heating induced in a DBS configuration. This model can be used to predict heating for different MR sequences, and enable a personalized safety margin to be implemented in the clinical protocol [15]. Safe scanning parameters produced by the model can directly be incorporated to scan a patient with little time delay. This prompts the following research question: *"How can we rapidly predict sequence-specific RF heating in DBS patients, and derive a personalized safety limit and associated MR acquisition parameters?"*

Chapter 2

Materials

Creating a model that can predict RF heating to enable safe clinical MRI scanning in DBS patients requires experimental data. This data is needed not only to validate the model, but also to calibrate it, the importance of which is highlighted in section 3.2.5. To acquire said data, a patient mimicking DBS phantom is constructed, details of which are described below. The phantom is scanned with various sequences (Table 3.1) using a 1.5T MRI scanner.

2.1 DBS Lead

In this study two DBS electrodes (Vercise Cartesia Directional, DB-2202, Boston Scientific, Marlborough, MA) are used to evaluate the RF heating. Each lead consist of 8 contact points: 6 directional and 2 ring electrodes. Additionally, the lead contains a marker which allows orientation evaluation based on CT imaging. [17]

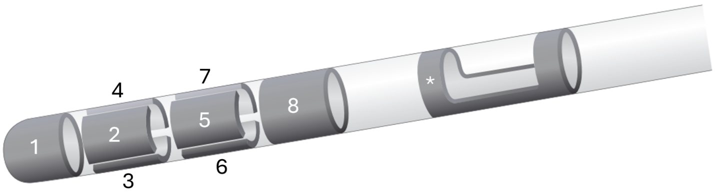

Figure 2.1: Boston Scientific Vercise Cartesia Directional lead DB 2202-30. Two ring (1&8) and 6 directional (2-7) electrodes. On the right a marker (denoted with *) to evaluate lead orientation based on CT imaging. [17]

2.2 Phantom Details

Using anthropomorphic phantoms is common practice in MRI research, where they are often utilized in sequence development, safety assessments and model calibration/validation. To produce valid results, it is critical these phantoms accurately mimic MRI-tissue interactions [6, 15, 16]. Parameters that typically require close resemblance are the dielectric properties, relaxation times, magnetic susceptibility and diffusive properties [18]. The phantom applied in this study consist of a head compartment as well as an upper torso. Both parts are 3D printed based on computer tomography images of a patient with a DBS system. The images were supplied by Northwestern University [6]. The skull is filled with gel, while the torso is filled with a saline solution. Both compartments are described in detail below.

2.2.1 Phantom Head

The skull model (Figure 2.2) was printed in two coronal halves using clear resin (Clear Photopolymer Resin V4, Formlabs, Berlin, Germany [19]). The halves were glued together and filled with gel.

Gel Filling

To obtain realistic results the dielectric properties of the gel must resemble that of brain tissue. The dielectric properties of grey and white matter at 1.5T (63.87 MHz) [20] are $\sigma = 0.51\ S/m$, $\epsilon_r = 98$ and $\sigma = 0.29\ S/m$, $\epsilon_r = 68$ respectively [21]. As the gel used is homogeneous; no distinction can be made between grey and white matter. A gel with electrical conductance of $\sigma = 0.32\ S/m$ and a permittivity of $\epsilon_r = 57.3$ is used to fill the skull [18].

Materials used to synthesize such gels are agar or agarose with saline solutions (Sodium Chloride NaCl) and permittivity lowering components, [6, 12, 15, 18] to which copper sulphate ($CuSO_4$) may be added to reduce T1 relaxation time [16]. Increasing gelling agent concentration reduces thermal conductivity [18, 22], while increasing salt levels increases electrical conductivity. To lower the permittivity, alcohol, sucrose, or polymers may be used [23]. In this phantom, polyvinylpyrrolidone (PVP) is used. PVP decreases the effect NaCl has on the electrical conductivity, thus a higher concentration must be used to achieve the same result [23]. Experimental data from the University of Leiden suggests that 70% PVP10 (Sigma Aldrich, the Netherlands [24]) and 1% NaCl (both w/w) are ideal [18]. This, in combination with 1.5% of agarose, results in an adequate gel of which 1.9 litres are used to fill the skull [6, 12, 16].

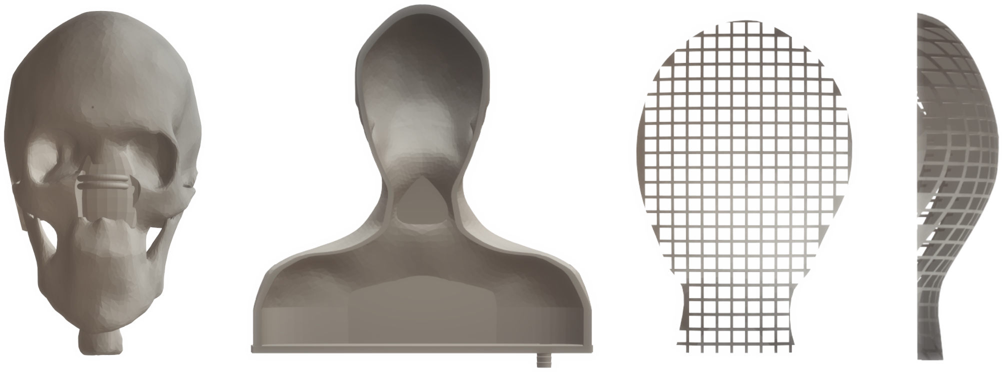

Figure 2.2: The model of the skull (left), the nasal cavity is filled up. In the middle, the model of the torso in which the skull is placed. A hose connection allows for easy drainage. A grid (right) is used to hold the skull in place. The finished phantom is depicted in Figure 2.6.

Electrode Orientation

In clinical settings, the electrode orientation comes very precise [5]. Different nuclei can serve as the target such as the Subthalamic Nuclei (STN), Globus Pallidus Interna and Caudate Nuclei [25, 26]. These areas are highlighted in Figure 2.3. As this phantom is a proof of concept, any of the above-mentioned areas is regarded a suitable location. The tips of the phantom DBS leads ended in the Subthalamic Nuclei.

Defining the entry-point through the skull leads to a fully constrained electrode trajectory (since it follows a straight line). Appropriate entry points can be seen in Figure 2.4. The boreholes in the phantom have a diameter of 3 mm.

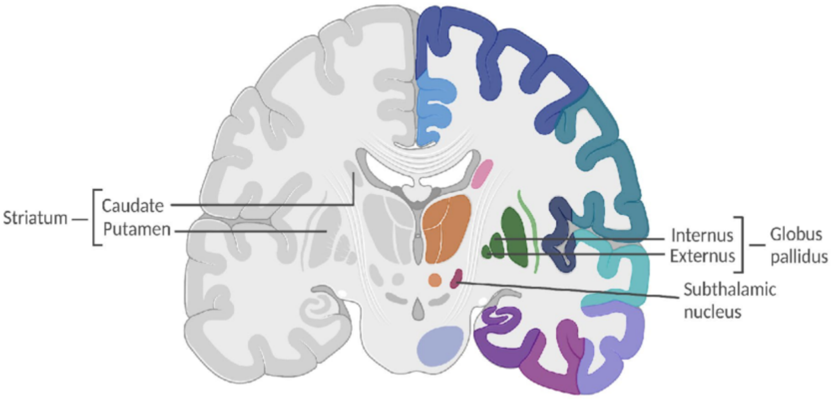

Figure 2.3: Coronal view of the human brain. Areas for DBS stimulation include the Subthalamic nucleus, Globus Pallidus Internal and Caudate Nucleus [25, 26, 27].

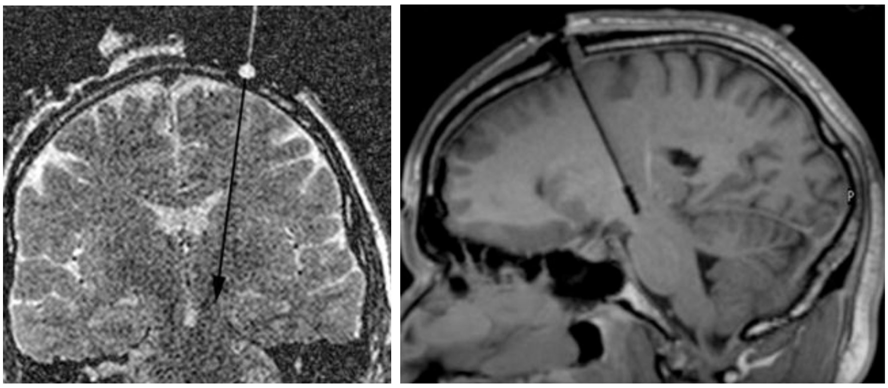

Figure 2.4: Borehole locations for treatment of Parkinson disease targeting the STN. On the left, an MRI scan taken during operation to assist alignment, right a post-operative MRI scan. Using these two images, the point of entry is defined. [28]

2.2.2 Phantom Torso

A torso was incorporated into the phantom mainly for two reasons. Firstly, the torso may influence the transmit RF field of the body coil [18]. Even if a head/neck coil is used as receiver, the torso still falls within the transmit RF field (Figure 2.5). Secondly, the antenna resonance effect on the electrode only appears when the size of the electrode is roughly half a wavelength. In air, the required lead length is almost 2 meters. However, as the magnetic waves propagate through the air into the human tissue, their wavelength shortens. Resonance will therefore occur at lead lengths around 20 centimetres [9].

The torso model is made of ABS through solid infill fused deposition modelling. It is printed as a single body (Xometry Europe, Germany [29]). A layer of epoxy is applied to the inside of the compartment to make the torso waterproof. To keep the head in place, a grid is fixed to the torso head compartment. Four pins from the back of the skull slide into this grid, ensuring consistent placement within the torso. An image of the setup is presented in Figure 2.6. To ensure phantom mobility, the torso design includes an outlet. This way the 18 litre torso can be filled while on the MRI table, and emptied after scanning [6]. The heating of the phantom was monitored in real-time using two fibre-optic temperature probes (see Figure 2.6)

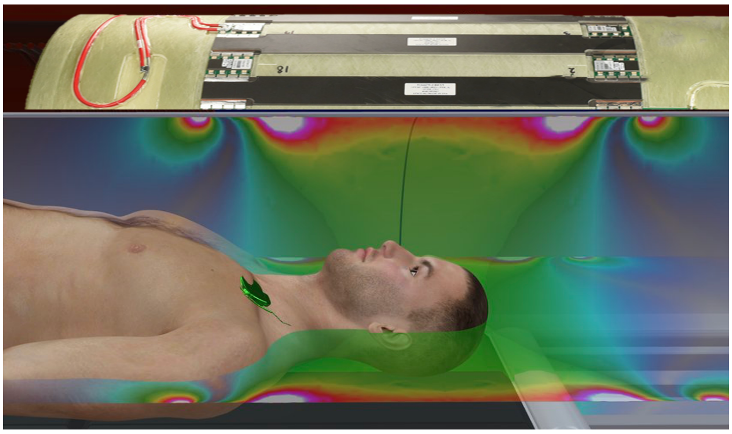

Figure 2.5: The transmit RF field of a body coil. When scanning the brain, the torso is partially inside the field as well. Hot spots appear near the edges of the coil.[30]

Figure 2.6: The phantom under the Siemens 20 channel head/neck scanning coil (left). The optical fibres are positioned at the tip of the leads (middle). The optical fibres penetrate the skull on the caudal end (right). Inside the skull they cross over to reach the lead at the opposing side to preserve lead orientation.

2.3 Thermometer

The two fibre-optic temperature probes are positioned at the tip of either lead (Figure 2.6) and connected to a TempSens signal conditioner [31]. The OpSense Solutions OTP-M temperature sensors have a calibrated range of 20-45 °C [32]. The signal conditioner has a similar operating temperature between 10-45 °C. This equipment is depicted in Figure 2.7.

Figure 2.7: The Tempsense (OpSens) thermometer with a sampling frequency of 50 Hz, a resolution of 0.1 °C and 0.3 °C accuracy (left). The tip of the OpSense Solutions OTP-M temperature probe (right). [31, 32]

Chapter 3

Methods

3.1 Phantom MRI measurements

The phantom was scanned using a Siemens Magnetom Aera 1.5T located at the University of Twente. Imaging was done using a body transmit coil and a 20 channel head/neck TIM (total imaging matrix) receiver coil (Figure 2.6). The phantom was placed in a supine position and entered the MRI head first.

3.1.1 Scan Protocols

Several scans were made including a GRE-pre-scan, various Fast spin echoes (FSE) and a lowSAR scan. Here, the GRE-pre-scan is used to evaluate the induced current. Three configurations were tested. In these configurations, the lead to the DBS electrode was positioned differently. The parameters for the scans are presented in table 3.1.

	Configuration 1					**Configuration 2**		**Configuration 3**	
Parameters	**FSE Cal**	**FSE 1**	**FSE 2**	**FSE 3**	**lowSAR**	**FSE**	**lowSAR**	**FSE**	**lowSAR**
TE [ms]	81	81	81	81	92	81	92	81	92
TR [ms]	2000	6000	4000	3000	7000	4000	6300	4000	4000
Flip angle [$degrees$]	150	150	150	150	120	150	120	150	120
$\mathbf{B_1}^+$**rms** [μT]	*	1.7	2.1	2.6	1.1	2.1	1.2	2.1	1.4
RF power [W]	106.1	35.4	53	70.7	11	52.3	12	52.3	18.9
Acquisition time [s]	600	300	200	150	168	200	150	200	90
Heating [$°C$]	22.3	6.2	8.8	10.9	1.5	8.0	1.5	6.5	2.2

Table 3.1: Table of sequence parameters for FSE and lowSAR scans in the tested configurations. Note that the value marked with an asterisk * was not recorded during the experiment.

3.1.2 Temperature measurement

To evaluate the heating process, the temperature was measured in real-time throughout the FSE-scans as well as several minutes after the scan took place. Before scanning again, the temperature was allowed to return to a baseline of approximately 22 degrees Celsius. Over the course of various scans, the phantom baseline temperature increased by 1.2 degrees. To compensate, the temperature curves were always determined with respect to their baselines.

3.2 Model

A model can be used to predict heating at the electrodes to find safe scanning parameters. Basic principles used in the model are first verified using a simplified thermodynamic equations model.

3.2.1 Pennes Bioheat Equation

Since its introduction in 1948, Pennes Bioheat equation has been utilized countless times in thermodynamic simulation that involve biological tissues [33, 34]. A recent Nature article on numerical simulation of RF heating of DBS implants employs it to calculate potential heating

[35]. In the context of this paper, the Bioheat equation is expressed as the following:

$$\rho C_p \frac{\partial T}{\partial t} = K \nabla^2 T + \rho \cdot SAR - b \cdot (T - T_b) \mid (x, y, z) \in \mathbb{R}^3,\ t \geq 0 \tag{3.1}$$

With boundary condition:

$$K \frac{\partial T}{\partial n} = -h \cdot (T - T_a) \tag{3.2}$$

Formula 3.1 describes the temperature change over time t. Here, ρ is density, C_p specific heat and K thermal conductivity of the tissue. The SAR term incorporates the RF heating at the electrodes. To simplify, heat loss due to blood flow b with blood temperature T_b is not included in the model (Equation 3.5). The boundary condition incorporates the heat-transfer coefficient h and the ambient temperature T_a to describe the changes in temperature T for a unit vector n normal to the surface.

3.2.2 Bioheat Equation Model

The following numeric model (Model 1) is inspired by the paper of fellow students and shows linearity, a concept later used in the minimum TR prediction model (Model 2, section 3.2.4). To model the heat dissipation from a point source in a homogeneous medium, such as an agar gel, formula 3.1 can be rewritten numerically.

A continues space-time function $F(x, y, z, t)$ can be written as $F(i\delta x, j\delta y, k\delta z, m\delta_t)$, where δ is the cell (the discretized element) size and δ_t is the incremental time step. The cell size is chosen uniform in every direction, $\delta x = \delta y = \delta z = \delta$. Therefore, the Laplacian of the temperature $\nabla^2 T$ in the i direction can be written as:

$$\nabla^2 T(i, j, k)_{ii} = \frac{1}{(i\delta)^2}(T(i+1, j, k) + T(i-1, j, k) - 2T(i, j, k)) \tag{3.3}$$

Here, the $i + 1$ denotes a cell positioned right of the currently calculated, and $i - 1$ a cell on the left. By using $-2T(i, j, k)$ the difference in heat is calculated. The same process can be applied to all directions:

$$\begin{aligned} \nabla^2 T(i, j, k) = \frac{1}{\delta^2}\Big[&T(i+1, j, k) + T(i-1, j, k) + T(i, j+1, k) \\ &+ T(i, j-1, k) + T(i, j, k+1) + T(i, j, k-1) - 6T(i, j, k)\Big] \end{aligned} \tag{3.4}$$

Substituting $\nabla^2 T$ into formula 3.1 for a homogeneous medium (no position variance or blood flow) the finite difference approximation becomes:

$$
\begin{aligned}
T^{m+1}(i,j,k) = T^{m}(i,j,k) + \frac{\delta t}{\rho C_p} Q + \\
\frac{\delta t \cdot K}{\rho C_p \delta^2} \cdot \Big[T(i+1,j,k) + T(i-1,j,k) + T(i,j+1,k) \\
+ T(i,j-1,k) + T(i,j,k+1) + T(i,j,k-1) - 6T(i,j,k) \Big]
\end{aligned}
\tag{3.5}
$$

Here, each cell is constructed using its previous temperature, the heat source Q and the heat transfer from its neighbours. The original model was constructed in MATLAB, however the model did not use matrix computations and the calculations required significant processing time. In this research, the existing model was sped up significantly using matrix computations rather than computing for every point. The boundary conditions for the x direction boils down to

$$
T^{m+1}(i_{min},j,k) = \frac{KT(i_{min}+1,j,k)}{K+h\delta} + \frac{T_a h + \delta K}{K+h\delta} \tag{3.6}
$$

Boundary conditions for both y and z directions can be computed similarly from formula 3.2.

3.2.3 Linearization

Using the model above, the temperature distribution can be determined for various input powers Q. From the temperature profiles, it becomes clear that, for a given moment in time, the heat follows the same distribution pattern. An illustration of this is provided in Figure 3.1. All the left 4 figures appear identical, but differ only in the intensity, as depicted by the colour bars. The power of the heating source only introduces a factor by which the heating is multiplied. Because the distribution patterns are identical, linearization of the heating process can be used to predict the temperature distribution for any power based on knowledge of the heat distribution at another power. This process requires only matrix scalar multiplications rather than a complete simulation, meaning the computation is sped up tremendously. The acquired relation holds for high power inputs ($Q > 10^5$), at which the error between the model and linear approximation remains well below 10^{-6} degrees Celsius.

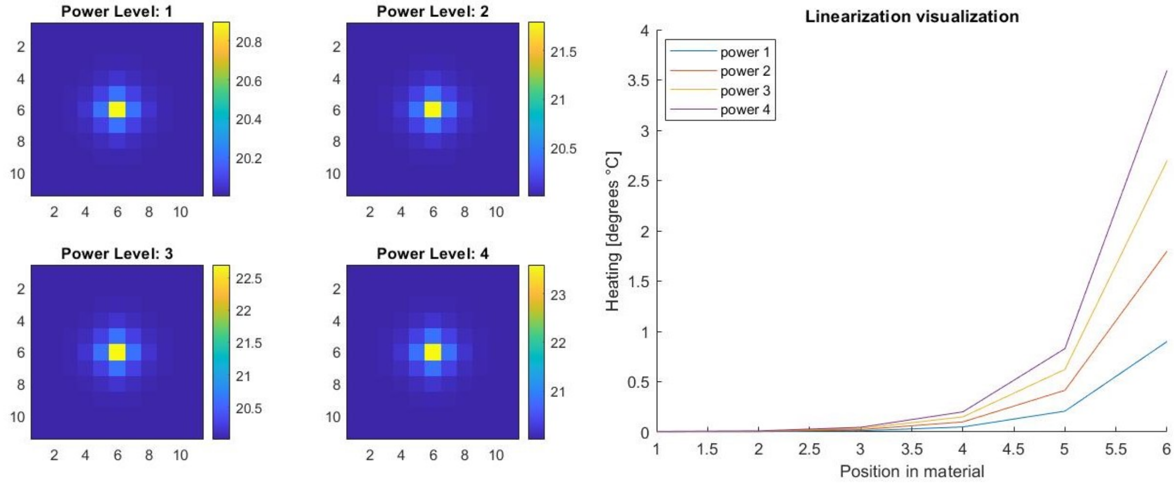

Figure 3.1: Temperature at the central slice for various power inputs, t = 900s (left). For visual clarity the simulation is run for an 11 sized cubic matrix rather than the actual 101 sized cubic matrix. A cross-section of the slice is depicted on the right, the Power 4 line is exactly four times the Power 1 line.

3.2.4 Minimum TR Prediction Model

Based on the linearity concept shown in Model 1, another model (Model 2), is constructed. This model takes in the induced current, which a Gradient Echo pre-scan provides. Based on this information and calibration data, the simulation ultimately predicts the temperature and compares it to a set maximum safe heating value (e.g. 2 degrees Celsius). It then returns the minimum TR needed to keep the heating caused by the sequence below that maximum value.

Certain principles govern Model 2. First and foremost, the power scaling concept of Model 1 (Figure 3.1) is utilized. The data of a longer period calibration scan can be scaled to calculate the temperature at other repetition times. This is clear from the following relation:

Model 1 linearization showed that for any point (x, y, x), at a given moment in time:

$$Temp(P_2) = Temp(P_1) \cdot \frac{P_2}{P_1} \tag{3.7}$$

Where P_2 is the power of scan 2 and P_1 the power for the calibration. Simply put, if one doubles the power, one doubles the temperature. A similar relation can be conducted for the TR using:

$$P \propto \frac{1}{TR} \tag{3.8}$$

And thus, when doubling TR, the temperature is halved conform the following relation:

$$Temp(TR_2) = Temp(TR_1) \cdot \frac{TR_1}{TR_2} \tag{3.9}$$

Another principle explored in the model is that the run time of the scan is the TR multiplied by the number of phase encoding steps (N_{pe}). This follows from the scanning mechanism of the MRI itself, in which each 'line' in the image plane is phase encoded and scanned separately. Simply put, the runtime is defined as:

$$runtime = TR \cdot N_{pe} \tag{3.10}$$

Combining knowledge of both principles, a simulation can use calibration data to determine the temperature at TR_x and scan time t_x (given parameter N_{pe}):

$$Temp(TR_x) = Temp(TR_1, t_x) \cdot \frac{TR_1}{TR_x} \bigg| \; t_x = TR_x \cdot N_{pe} \tag{3.11}$$

To find a scan where the end temperature stays below the given boundary temperature, the model iteratively adjusts from a base value. Shortly put, the model uses information of past calculations to narrow the TR boundaries within which the desired TR may be found. The TR_x for which the temperature is determined will be given by:

$$TR_x = \frac{U_B + L_B}{2} \tag{3.12}$$

Where U_B and L_B denote the upper and lower bound respectively. After each attempt, the boundaries are adjusted based on the outcome temperature. If the temperature surpassed the max temperature, the new upper bound is the previous TR_x. Similarly, if the temperature was below the max, the new lower bound is set to TR_x. In this manner, the TR for which the max temperature is reached is found promptly. Conform the Binary search algorithm [36], the maximum number of guesses (g) needed is given by:

$$g = \lceil \log_2 n \rceil \tag{3.13}$$

Here n is the size of the data scope. For example at TR = 6000ms, with an accuracy of 1ms this means the max number of guesses needed is 13. A visual representation of the calculation process is depicted in Figure 3.2.

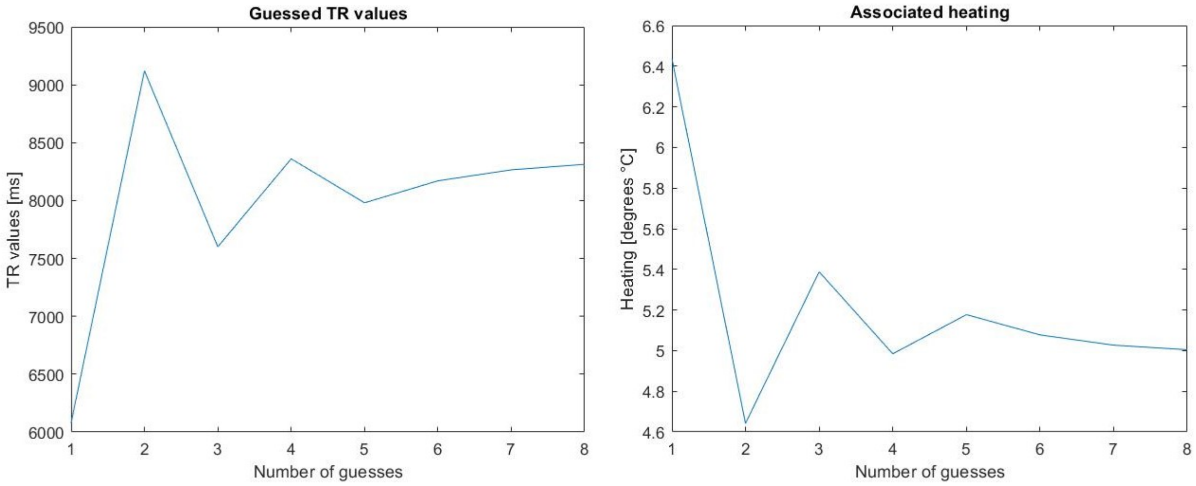

Figure 3.2: The iterative process of estimating a suitable TR value. Here, a boundary temperature of 5.00 degrees is chosen. The minimum TR value is a repetition time of 8350 ms.

3.2.5 Calibration Versatility

Calibration scans are long and too SAR intensive to be acquired from a patient. Therefore, they must be made beforehand on an anthropomorphic phantom or cadaver. To translate the calibration from the configuration of the phantom/cadaver to that of the patient, one additional step is required. The calibration is scaled using the induced current data from the GRE scan (Appendix A). Namely, the resulting heating power is proportional to the square of the induced current: $P \propto I^2$. Therefore, if the induced current is doubled, the calibration curve must be quadrupled to suit the new situation.

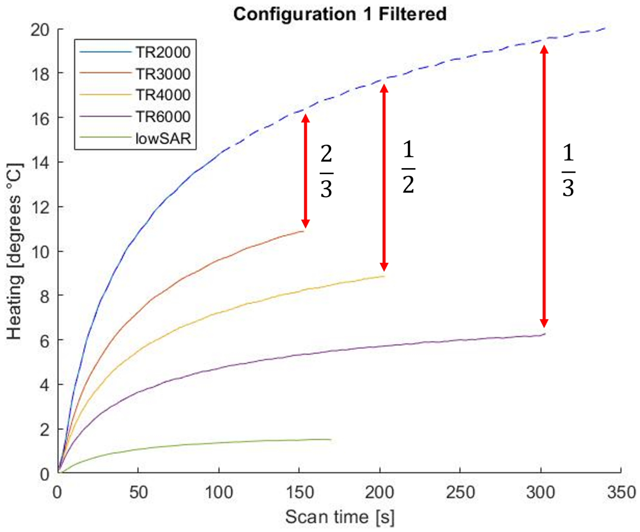

Figure 3.3: An example of how a calibration line can be used to predict the end temperature at other TR's. Note that the calibration was scanned using 6 consecutive sequences with a TR of 2000 ms, resulting in large heating. For illustrative purposes, only the first 350 seconds of the calibration scan are depicted. A scaling factor of $\frac{1}{2}$ can be found between TR 2000 and TR 4000 using $\frac{TR_{calibration}}{TR_{desired}}$. Similarly, the other scaling factors are found to be $\frac{2}{3}$ and $\frac{1}{3}$.

Chapter 4

Results

4.1 Phantom Results

4.1.1 GRE scan

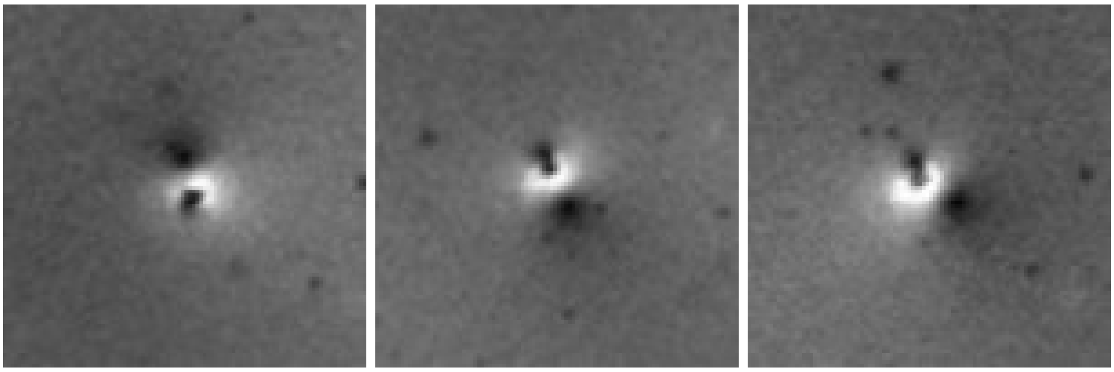

Figure 4.1: Cropped 3D GRE-scan images. Left to right configurations 1, 2 and 3 respectively. Induced current can be evaluated using a script of University of Twente (see appendix A) [15].

Configuration	**1**	**2**	**3**
Relative $\mathbf{I_{induced}}$	100%	95.1%	84.5%
Relative Power	100%	90.5%	71.4%

Table 4.1: The induced currents relative to the current experienced in configuration 1. The relative power, which is the square of the relative current, is used to scale the calibration curve obtained in configuration 1. The scaled calibration curve is used to predict the temperature for other configurations (Figure 4.4).

4.1.2 Configurations

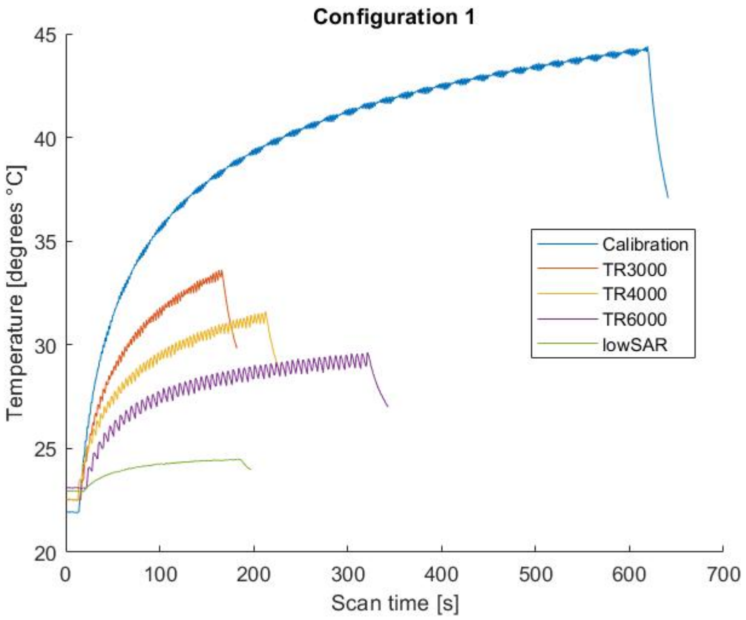

Figure 4.2: Unfiltered experimental data from configuration 1. A zigzag artefact follows the frequency of the repetition time. When the scanner is pulsing, the temperature rapidly increases. During the waiting period, the temperature decreases. At lower TR's, the frequency of the zigzag increases accordingly. Visible on the calibration line is another artefact. Here, the TR is close to the sampling frequency of the temperature probes. The sampling going in and out of phase causes an extra frequency to be multiplied with the zigzag artefact.

Artefacts are caused by the TR and sampling frequency, as shown in Figure 4.2. These artefacts are undesired when applying the calibration curve to predict temperature curves for other sequences. Therefore a filter is applied that removes the undesired frequencies and smooths the curve using a moving average (Figure 4.3). Details are provided in appendix B.

LowSAR

The lowSAR (Siemens) sequences use max excitation pulse amplitudes, which results in lower heating. A factor of around 3 is found between a lowSAR and normal FSE for the same configuration and TR. This factor is used in the prediction of the lowSAR temperatures in Table 4.2 and Figure 4.5.

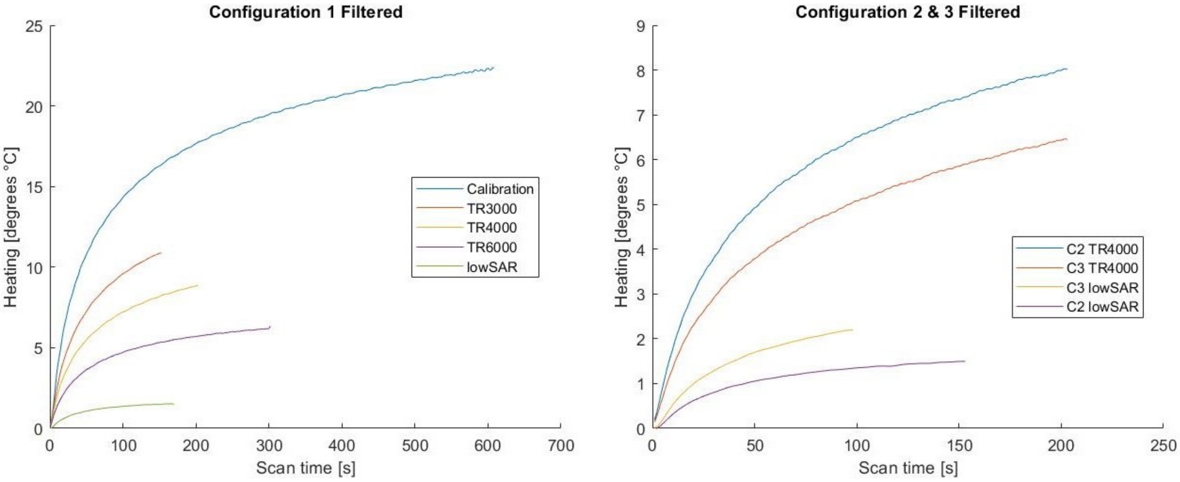

Figure 4.3: Left, scan data for configuration 1. Note that the repetition time of the calibration and lowSAR scan are 2000 ms and 7000 ms respectively. On the right, the scan data for configuration 2 and 3. The lowSAR scans used a repetition time of 6300 ms and 4000 ms respectively (see Table 3.1).

4.2 Model Results

Using the calibration and the induced current values (see table 4.1), the heating curves are predicted for all configurations. Comparisons between actual data and predictions are displayed below (Figure 4.4).

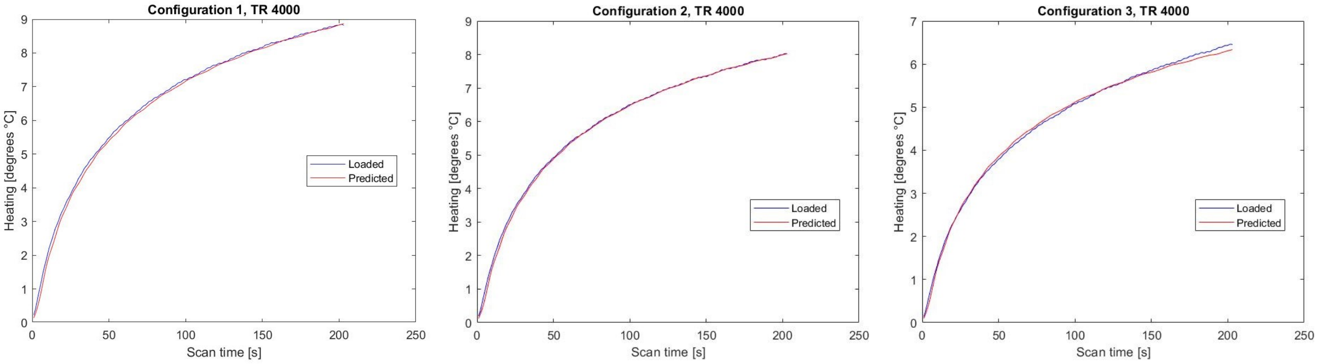

Figure 4.4: Heating curve predictions and their measured counterparts. Note that for configuration 1 and 2, the prediction shows high conformity to the measured data. For configuration 3, the lines start diverging after approximately 150 seconds.

Parameters		**Configuration 1**	
TR $[ms]$	**Scantime** $[s]$	$\mathbf{T_{FSE}}$ $[°C]$	$\mathbf{T_{lowSAR}}$ $[°C]$
3400	170	10	3.3
3600	180	9.5	3.2
3900	190	9	3.0
4200	210	8.5	2.8
4600	230	8	2.7
5000	250	7.5	2.5
5400	270	7	2.3
6000	300	6.5	2.2
6600	330	6	2.0
7400	370	5.5	1.8
8300	420	5	1.7
9500	470	4.5	1.5
10900	550	4	1.3

Table 4.2: Temperature predictions for configuration 1 based on the calibration data. The lowSAR sequence results in roughly $\frac{1}{3}$ of the heating of the FSE. According to the prediction, heating of 2 degrees in configuration 1 may be acquired with a lowSAR scan with TR $>$ 6600 ms. Experimental data suggests this may be achieved with a lower TR (table 3.1).

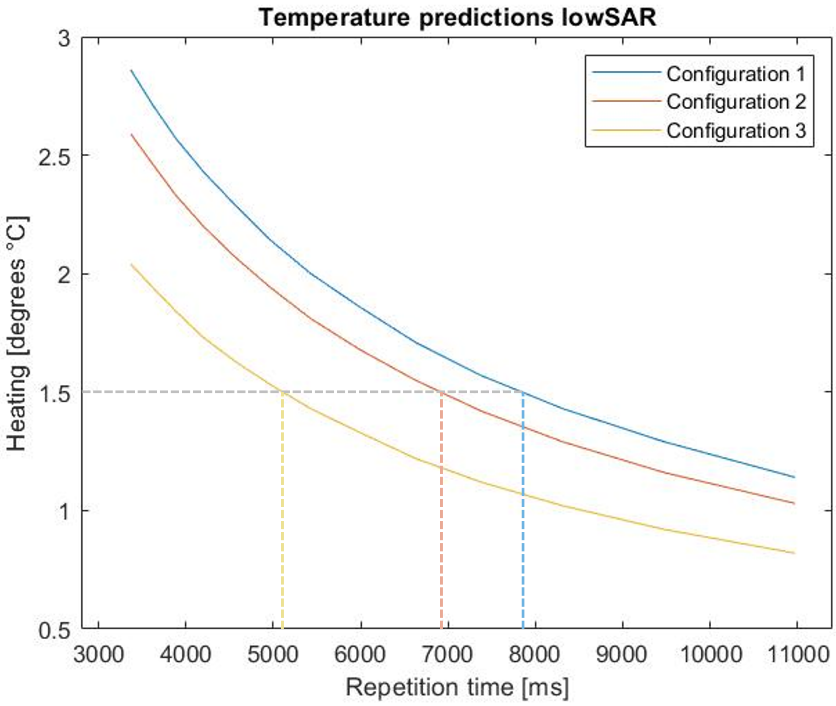

Figure 4.5: LowSAR predictions made using induced current data (Table 4.1) to scale configuration 1 calibration data. Given a maximum heating (e.g. 1.5 degrees), the associated repetition times can be found. Depending on the configuration, the minimum TR may vary.

Chapter 5

Discussion

Modelling RF heating in DBS patients to rapidly determine safe scan parameters may prove vital to facilitate clinical MR imaging on said patients. A method of predicting the minimum safe repetition time was explored within this paper. By scaling calibration curves, large simulations were avoided, thus speeding up the process. Calibration data was obtained from an anthropomorphic phantom of a head and torso, scanned at 1.5T. This calibration data was scaled using details on the induced current provided by GRE scans. Scaled calibration curves were compared to experimental data to validate the approach.

In this report, it was shown that scaling calibration data can provide an accurate estimation of the heating process not only within a configuration, but it also translates to other configurations. Using a low SAR GRE scan prior to the diagnostic scan, all necessary scaling data may be acquired. A simple binary-search like algorithm can then rapidly find the minimum required TR for a given sequence. The repetition time is calculated by the model in less than 10 ms (excluding GRE scan interpretation), allowing quick incorporation into a scanning protocol.

Over the years, various simulations have been made of RF heating around DBS electrodes. These simulations have been validated in phantoms, and recently in cadavers [37]. When aiming for higher accuracy simulations, computation time may rapidly increase. For example, this paper's initial bioheat model was constructed for an 11 sized cubic matrix and had a run time of mere seconds. When scaling this up to a 101 size cubic matrix, the computations became tedious, especially when calculating for various powers and time periods. By improving the code for the language used (MATLAB), computation time was significantly reduced. However, by scaling calibration data instead, these computations may be avoided all together. So while providing valuable information on the heating process, simulations lack the speed required for clinical viability. Post-operative scanning desires a smooth workflow in which lengthy simulations cannot take place. Additionally, high accuracy simulations require detailed information on e.g. the DBS lead, information which may not be provided by the manufacturer. A calibration scan does not require any sensitive information, but must be recorded for every lead type. As the heating at the tip is generally speaking the only point of interest, storage space should not be limiting.

As a calibration curve is used to predict other heating curves, discrepancies between the experimental setup and the in vivo situation will be transferred to the results of the model. To provide accurate and representative data, the phantom must express high levels of anthropomorphism. While this paper's phantom has an accurate shape and representative dielectric properties, there are various differences from the in vivo situation.

Most obvious is the homogeneous nature of the phantom. The brain of the phantom is filled with a single mixture rather than two separate ones representing white and grey matter. Additionally, the thorax is filled with a saline solution which does not represent the tissue transitions around the lead as found in patients. The importance of representative layers was illustrated by Bhumi Bhusal et al. (2021) while investigating the effect of subcutaneous fat on the heating process [6]. Finally, heat perfusion through blood vessels is also not incorporated. Since perfusion has a mitigating effect on the temperature of its surroundings, in vivo conditions may be safer than measured in the phantom [38]. All in all, steps could be made to make the phantom more anthropomorphic. However, as shown by Eryaman et al. the linearity concepts may also be projected onto cadavers [37]. This suggests that the proof of concept that this paper provides may still be applicable in vivo.

It is important to note that, while the phantom included two leads and two probes, data is only depicted of the anatomical left lead. This lead showed much greater heating than its neighbouring lead. All relations hold and the scaling factors between the measurements are maintained for both leads. However, as the right lead showed a heating of sometimes less than 10% of that of the left lead (both anatomically), the signal-to-noise ratio was unfavourable. The difference in heating of the leads, was caused by different lead lengths, positions and orientations in the RF field.

The model described in this paper aims to accurately predict the heating at the tip of the electrode using calibration scan data. Unfortunately, the model loses accuracy when predicting for sequences with long repetition times (TR 6000 configuration 1) as well as configurations that experience little heating (configuration 3, Figure 4.4). This is likely because variables assumed to be constant, vary slightly as the temperature increases. By making a calibration scan that results in more clinically representative heating, this effect may be reduced. This is especially important in vivo, where parameters such as blood perfusion may vary as temperature increases.

For a model to become clinically viable, various steps must be taken. Firstly, the model must be validated extensively to ensure safety of the patients. Secondly, the model must be fully automated. GRE scan images must be automatically loaded, processed, the calibration scaled and safe parameters determined. Only then can the process be fast enough to ensure smooth operation within scanning procedures. Additionally, models such as the one explored in this paper find great benefit in collaboration with SAR minimizing simulations. Such simulations can significantly reduce heating on bilateral DBS leads [2, 39]. Especially when one lead experiences much more heating than the other, as a minimizing approach can even this out, resulting in lower peak heating. This allows for safe, quick and high quality scanning for DBS patients.

Chapter 6

Conclusion

In this paper, a method of predicting RF Heating was explored for use in MRI scanning of DBS patients. It was shown that the temperature is inverse linearly dependent on the repetition time. A calibration measurement on a phantom may be used to predict heating, both in a single electrode-lead-configuration, as in other DBS configurations. A low SAR 3D GRE-scan can provide the necessary information to scale between these configurations. Combined with SAR minimizing methods, a simulation as described in this paper may allow for safe and adequate clinical MRI scans for DBS patients.

Bibliography

[1] Chima O. Oluigbo and Ali R. Rezai. Chapter 7 - magnetic resonance imaging safety of deep brain stimulator devices. 116:73–76, 2013.

[2] Yigitcan Eryaman, Naoharu Kobayashi, Sean Moen, Joshua Aman, Andrea Grant, J. Thomas Vaughan, Gregory Molnar, Michael C. Park, Jerrold Vitek, Gregor Adriany, Kamil Ugurbil, and Noam Harel. A simple geometric analysis method for measuring and mitigating rf induced currents on deep brain stimulation leads by multichannel transmission/reception. *NeuroImage*, 184:658–668, 2019.

[3] Gupta V. Fariba KA. *Deep Brain Stimulation.* Treasure Island (FL): Statpearls Publishing, 2023.

[4] Paul E. Holtzheimer and Helen S. Mayberg. Deep brain stimulation for psychiatric disorders. *Annual Review of Neuroscience*, 34:289–307, 2011.

[5] Maarten Bot, P Richard Schuurman, Vincent J J Odekerken, Rens Verhagen, Fiorella Maria Contarino, Rob M A De Bie, and Pepijn van den Munckhof. Deep brain stimulation for parkinson's disease: defining the optimal location within the subthalamic nucleus. *Journal of Neurology, Neurosurgery & Psychiatry*, 89(5):493–498, 2018.

[6] Bhumi Bhusal, Bach T. Nguyen, Pia P. Sanpitak, Jasmine Vu, Behzad Elahi, Joshua Rosenow, Mark J. Nolt, Roberto Lopez-Rosado, Julie Pilitsis, Marisa DiMarzio, and Laleh Golestanirad. Effect of device configuration and patient's body composition on the rf heating and nonsusceptibility artifact of deep brain stimulation implants during mri at 1.5t and 3t. *Journal of Magnetic Resonance Imaging*, 53(2):599–610, 2021.

[7] Sarah Christina Reitz, Janina Lemmer-Etzrodt, Michael Eibach, Ferdinand Bohmann, Fee Keil, Nazife Dinc, Nikhil Thakur, Jun-Suk Kang, Lutz Weise, Volker Seifert, Marcus Czabanka, Simon Baudrexel, and Johanna Quick-Weller. Necessity of mri-compatible deep brain stimulation systems - hits and hints for decision making. *Clinical neurology and neurosurgery*, 224:107514, January 2023.

[8] Jaimie Henderson, Jean Tkach, Michael Phillips, Kenneth Baker, Frank Shellock, and Ali Rezai. Permanent neurological deficit related to magnetic resonance imaging in a patient with implanted deep brain stimulation electrodes for parkinson's disease: Case report. *Neurosurgery*, 57:E1063; discussion E1063, December 2005.

[9] Marcus C. Bennett, David B. Wiant, Jacob A. Gersh, Wendy Dolesh, X. Ding, Ryan C. M. Best, and J. D. Bourland. Mechanisms and prevention of thermal injury from gamma radiosurgery headframes during 3t mr imaging. *Journal of Applied Clinical Medical Physics*, 13(4):54–70, 2012.

[10] Robert W. Gray, W. Timothy Bibens, and Frank G. Shellock. Simple design changes to wires to substantially reduce mri-induced heating at 1.5 t: implications for implanted leads. *Magnetic Resonance Imaging*, 23(8):887–891, 2005.

[11] Peter Serano, Leonardo Angelone, Husam Katnani, Emad Eskandar, and Giorgio Bonmassar. A novel brain stimulation technology provides compatibility with mri. *Scientific reports*, 5:9805, April 2015.

[12] Laleh Golestanirad, Ehsan Kazemivalipour, Boris Keil, Sean Downs, John Kirsch, Behzad Elahi, Julie Pilitsis, and Lawrence L. Wald. Reconfigurable mri coil technology can substantially reduce rf heating of deep brain stimulation implants: First in-vitro study of rf heating reduction in bilateral dbs leads at 1.5 t. *Plos One*, 14(8):1–17, August 2019.

[13] Yigitcan Eryaman, Burak Akin, and Ergin Atalar. Reduction of implant rf heating through modification of transmit coil electric field. *Magnetic Resonance in Medicine*, 65(5):1305–1313, 2011.

[14] Hanno Homann, Ingmar Grässlin, Holger Eggers, Kay Nehrke, Peter Vernickel, Ulrich Katscher, Olaf Dössel, and Peter Börnert. Local sar management by rf shimming: A simulation study with multiple human body models. *Magma (New York, N.Y.)*, 25:193–204, September 2011.

[15] W. Roskamp. Rf heating mitigation around a dbs lead at 3t, May 2023.

[16] Nur Izzati Huda Zulkarnain, Alireza Sadeghi-Tarakameh, Jeromy Thotland, Noam Harel, and Yigitcan Eryaman. A workflow for predicting radiofrequency-induced heating around bilateral deep brain stimulation electrodes in mri. *Medical Physics*, 51(2):1007–1018, 2024.

[17] Boston Scientific. Neuromodulation deep brain stimulation systems, 2020. Accessed: 2024-06-07.

[18] Wyger Maurits Brink, Zhiyi Wu, and Andrew Webb. A simple head-sized phantom for realistic static and radiofrequency characterization at high fields. *Magnetic Resonance in Medicine*, 80, March 2018.

[19] Formlabs. Clear resin v4, 2024.

[20] Joseph P. Hornak. *The Basics of MRI*, chapter 3. Spin Physics. January 2010.

[21] Di Gennaro F. Baumgartner C. Neufeld E. Lloyd B. Gosselin M.C. Hasgall, P.A. It'is database for thermal and electromagnetic parameters of biological tissues, February 2022.

[22] Min Zhang, Zhenhua Che, Jianhua Chen, Huizhong Zhao, Le Yang, Zhiyou Zhong, and Jiahua Lu. Experimental determination of thermal conductivity of wateragar gel at different concentrations and temperatures. *Journal of Chemical & Engineering Data*, 56(4):859–864, 2011.

[23] Carlotta Ianniello, Jacco A. de Zwart, Qi Duan, Cem M. Deniz, Leeor Alon, Jae-Seung Lee, Riccardo Lattanzi, and Ryan Brown. Synthesized tissue-equivalent dielectric phantoms using salt and polyvinylpyrrolidone solutions. *Magnetic Resonance in Medicine*, 80(1):413–419, 2018.

[24] Sigma Aldrich. Polyvinylpyrrolidone (pvp10), 2024.

[25] Hui Li, Dapeng Li, Wuyang Yang, Huifang Yan, Zifang Zhao, and Haibo Yang. Deep brain stimulation (dbs) with subthalamic nucleus (stn) as target for pediatric patients with pkan. *World Neurosurgery*, 163:e317–e322, 2022.

[26] Philip Perez, Sarah Wang, Susan Heath, Jennifer Henderson Sabes, Danielle Mizuiri, Leighton Hinkley, Srikantan Nagarajan, Paul Larson, and Steven Cheung. Human caudate nucleus subdivisions in tinnitus modulation. *Journal of Neurosurgery*, 132:1–7, February 2019.

[27] Ayush Tripathi, Rajagopal Appavu, and Jothsna Kethar. The age of the meta-doctor: Diagnosing parkinson's disease with artificial intelligence and speech. *Journal of Student Research*, 12, May 2023.

[28] Philip Starr, Alastair Martin, Jill Ostrem, Pekka Talke, Nadja Levesque, and Paul Larson. Subthalamic nucleus deep brain stimulator placement using high-field interventional magnetic resonance imaging and a skull-mounted aiming device: Technique and application accuracy - clinical article. *Journal of neurosurgery*, 112:479–90, September 2009.

[29] Xometry Europe. Fused deposition modeling (fdm) services, May 2024.

[30] Kanal E. Rf fields overview, 2020. Accessed: 2024-06-21.

[31] Althen Sensors & Controls. Opsense 4-channel tempsens datasheet, 2015. Accessed: 2024-06-03.

[32] OpSense Solutions. Otp-m fiber optic high accuracy temperature sensor. Accessed: 2024-06-07.

[33] Eugene H. Wissler. Pennes' 1948 paper revisited. *Journal of Applied Physiology*, 85(1):35–41, 1998. PMID: 9655751.

[34] Jianqing Wang and Fujiwara Osamu. Fdtd computation of temperature rise in the human head for portable telephones. *IEEE Transactions on Microwave Theory and Techniques*, 47(8):1528–1534, 1999.

[35] C. McElcheran, Laleh Golestanirad, Maria Ida Iacono, P.-S Wei, B. Yang, K. Anderson, Giorgio Bonmassar, and S. Graham. Numerical simulations of realistic lead trajectories and an experimental verification support the efficacy of parallel radiofrequency transmission to reduce heating of deep brain stimulation implants during mri. *Scientific Reports*, 9:2124, February 2019.

[36] Will Vincent. Algorithms: Binary search, May 2017. Accessed: 2024-06-12.

[37] Dee M Koski Noam Harel Yigitcan Eryaman Nur Izzati Huda Zulkarnain-Lemke, Alireza Sadeghi-Tarakameh. In-vivo validation of a workflow to predict heating around a deep brain stimulation contacts. In *Proceedings of the 33rd Annual Meeting of ISMRM*, page 3721, 2024. Center for Magnetic Resonance Research (CMRR), University of Minnesota, Minneapolis, United States.

[38] Mingming Zhu, Joseph J.H. Ackerman, and Dmitriy A. Yablonskiy. Body and brain temperature coupling: The critical role of cerebral blood flow. *Journal of Comparative Physiology B: Biochemical, Systemic, and Environmental Physiology*, 179(6):701–710, 2009.

[39] R.S. Vinke-M. van der Graaf W.M. Brink C.D.E. van Speybroeck, W. Roskamp. reduction of rf-heating on bilateral dbs leads using two channel rf-shimming on 3t mri. In *Proceedings of the 33rd Annual Meeting of ISMRM*, page 3726, 2024.

[40] Christopher M. Collins and Zhangwei Wang. Calculation of radiofrequency electromagnetic fields and their effects in mri of human subjects. *Magnetic Resonance in Medicine*, 65(5):1470–1482, 2011.

[41] E.M. Purcell and D.J. Morin. *Electricity and Magnetism*. Cambridge University Press, 3 edition, 2013. Accessed online.

Appendix A

Induced Current Method

The RF field used in MRI scanning can induce a current on metallic leads. This current is responsible for the heating found at the tip of the electrodes in DBS patients. Characterization of this current gives insight in the heating process and allows for mitigation strategies. Characterization requires two aspects of the current, the magnitude and the phase. The phase gives important information for mitigation strategies [2, 15], but serves no purpose in scaling the calibration as done in this paper. Therefore, it is only briefly discussed below.

To find the magnitude and phase of the induced current, one can utilize the transmit null artifact (Tx_{null}). As follows from the Maxwell equations, the induced current on the lead produces a concentric magnetic field around the lead [40]. As the field strength decreases with distance from the lead, there will be distance at which the magnitude of the induced field matches that of the transmit field (B_1^+). At the point where these fields are in opposite directions, they cancel out, resulting in the Tx_{null} artifact. The distance between the lead and the artifact r gives insight in the magnitude of the current, while the angle ϕ the artifact makes (see Figure A.1) communicates the phase.

Following from the Biot-Sarvart law, the analytical field solution over an infinite wire is [41]:

$$B = \frac{\mu_0 \cdot I}{2\pi \cdot r} \tag{A.1}$$

Where B is the magnetic field strength perpendicular to the wire, μ_0 the magnetic permittivity in vacuum, I the current on the wire and r the distance from the wire. If the magnetic field B is to cancel the transmit field B_1^+, then I must be [2]:

$$|I_{ind}| = \frac{|B_1^+| 4\pi r}{\mu_0} \tag{A.2}$$

In order to find B_1^+, the magnetic field can be assessed underneath the tip of the electrode following Eryamans work [2]. In this paper, the B_1^+ are assumed constant. Therefore, since the relative current is desired, various calculation steps are no longer required. The relative induction current is then given by:

$$I_1 = I_0 \frac{r_1}{r_0} \tag{A.3}$$

Where I_1 and I_0 are the induced currents in the scan and calibration configuration respectively. r_1 and r_0 are their respective radii in the GRE image.

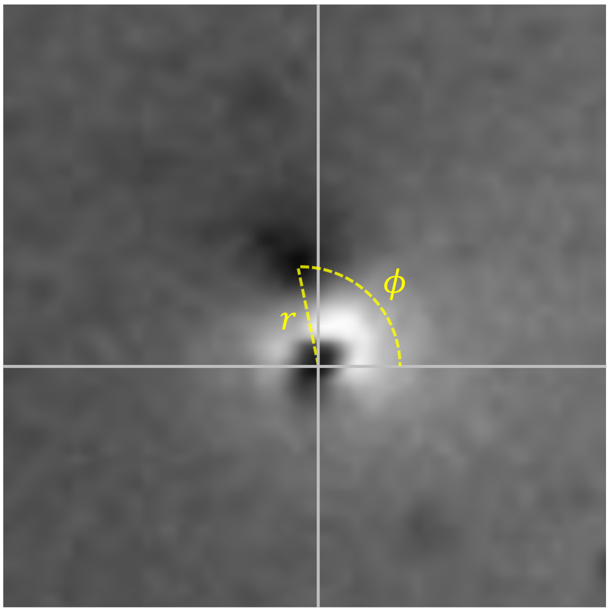

Figure A.1: A cropped GRE scan of the anatomical left lead in configuration 1. The lead is set as the centre of the coordinate system, distances and angles are determined with respect to it. The distance r carries information regarding the magnitude of the induced current. The angle ϕ carries information on the respective phase.

Appendix B

Filter

As illustrated in Figure 4.2, the data requires processing and filtering. Aspects to address are the baseline and the unwanted frequencies of the TR vibration and probe sampling artifact.

The baseline at which each measurement began is not constant. While 10 minutes was taken to allow the phantom to cool, the start temperature of 21.9 degrees was not reached. To fairly compare the data, the baseline was subtracted for each sequence. The resulting data therefore showed the heating rather than the temperature of the sample. To calculate the baseline, the temperature data (approximately 10 seconds prior to the start of the scan) was averaged.

In order to remove the undesired frequencies, the signal was filtered in the Fourier domain. To preserve the shape of the function at the transition points, the signal was extended. This means that it was zero padded at the start, and the final temperature value at the end of the scan was extended briefly. Additionally, MATLAB's moving average function (movmean of window length 5) was used to further smooth the curve. Comparisons of the filtered and non-filtered data are given below. In all cases, regardless of the heating (and thus signal-to-noise ratio), the filter functions adequately.

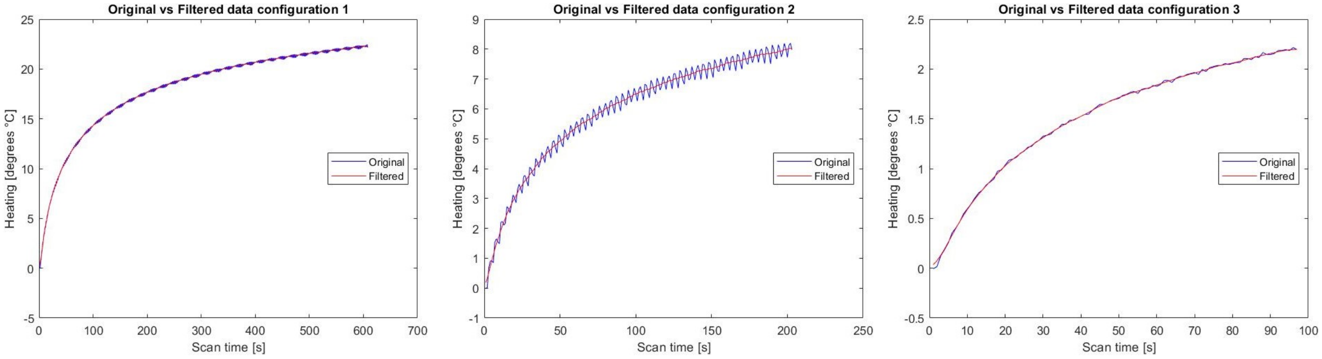

Figure B.1: Comparison between measured (original) and filtered data. On the left, the calibration scan at TR2000 in configuration 1. In the middle, the TR4000 scan in configuration 2. On the right, the lowSAR of configuration 3.